Interfacial Mott State in Iridate-Nickelate Superlattices

Xiaoran Liu,[1,][*] M. Kotiuga,[1] H.-S. Kim,[1] Alpha T. N'Diaye,[2] Y. Choi,[3] Yanwei Cao,[4] M. Kareev,[1] F. Wen,[1] B. Pal,[1] J. W. Freeland,[3] D. Haskel,[3] P. Shafer,[2] E. Arenholz,[2] K. Haule,[1] David Vanderbilt,[1] Karin M. Rabe,[1] and J. Chakhalian[1]

[1]*Department of Physics and Astronomy, Rutgers University, Piscataway, New Jersey 08854, USA*
[2]*Advanced Light Source, Lawrence Berkeley National Laboratory, Berkeley, California 94720, USA*
[3]*Advanced Photon Source, Argonne National Laboratory, Argonne, Illinois 60439, USA*
[4]*Ningbo Institute of Materials Technology and Engineering,*
Chinese Academy of Sciences, Ningbo, Zhejiang 315201, China

In new $SrIrO_3/LaNiO_3$ superlattices up to a full electron transfer at the interface from Ir to Ni is experimentally observed, triggering a massive structural and electronic reconstruction. The large crystal field splitting from the distorted interfacial IrO_6 octahedra surprisingly dominates over the spin-orbit coupling, and together with the Hund's coupling results in the high-spin ($S = 1$) configurations on both Ir and Ni sites. First-principles calculations agree well with the experimental results, supporting the formation of an intricate Mott state in the superlattices.

The ability to construct heterostructures in a layer by layer way provides the opportunity to combine properties of multiple materials together and generate emergent quantum states that deviate considerably from individual components [1]. A major knob towards this goal, interfacial charge transfer (ICT), well known to occur in conventional semiconductor/metal heterojunctions due to the work function mismatch, can lead to exotic scenarios in complex oxide heterostructures [2]. In particular, strong electron-electron correlations can couple the charge with lattice, orbital, and/or spin degrees of freedom, potentially modifying the structural, electronic and magnetic properties of constituent materials at the interface [2–5].

While the majority of previous studies on ICT were focused on materials with $3d$ and $4d$ transition metal oxides [6], lately the $5d$ iridates have come to the fore. Their strong spin-orbit coupling (SOC) of ∼0.5 eV, comparable to the on-site Coulomb repulsion U and crystal field (CF) splitting Δ_{CF} [7–11], set them as a promising playground to host interesting quantum phases including relativistic SOC Mott insulator [7], topological insulator [12–14], unconventional superconductivity [15–17] and Weyl semimetal [18]. ICT in those compounds provides a potentially useful mechanism to create novel interfacial phases, as revealed recently in iridate-manganite systems [19–21]. Nevertheless, such an effect was absent in many other iridate-based artificial heterostructures and superlattices [22–29].

To engineer the ICT involving an iridate, where the Ir $5d$- and O $2p$-orbitals have a large on-site energy difference (∼1 eV), it is appealing to interface it with a $3d$ rare-earth nickelate, $RNiO_3$ [30], a negative charge transfer material characterized by the formation of oxygen ligand holes akin to those found in high T_C cuprates [31, 32] where the order of the Ni $3d$ and O $2p$ levels is inverted. Thus, a large ICT is anticipated from the Ir $5d$-orbital to the Ni $3d$-orbital from a simple potential energy argument in which the O $2p$-bands are aligned at the interface [33, 34]. However, the realization of such an effect should call into question the adequacy of the 'band bending' picture often employed in the presence of ICT [35] and the conventional view of iridates as dominated by strong SOC and as a relativistic Mott insulating state in the ultra-thin limit [23, 36–38].

In this Letter, we present experimental and theoretical results on $(SrIrO_3)_m/(LaNiO_3)_n$ ("mS/nL") superlattices (here m and n refer to the number of $SrIrO_3$ and $LaNiO_3$ unit cells, respectively) specifically designed to address those issues. $SrIrO_3$ is an exotic semimetal due to its intrinsic strong SOC [39, 40], whereas $LaNiO_3$ is the unique member of $RNiO_3$ family with a paramagnetic metallic state down to the lowest temperature [30] [Fig. 1(a)]. For the superlattices studied, a clear metal-to-insulator crossover is observed as m and n are reduced to only a few unit cells. Strikingly, we find the signature of a massive electron transfer of ∼$1e$ per Ir/Ni interfacial pair switching the electronic configurations from $5d^5/3d^7$ to $5d^4/3d^8$. This effect not only redefines the charge distribution, but also expands the NiO_6 and compresses the IrO_6 octahedra [Fig. 1(b)]. As a result, the system is driven away from the strong SOC limit towards an atypical interfacial Mott state with $S = 1$ high-spin configuration on both Ni and Ir sites [Fig. 1(c)-(f)]. These findings demonstrate how, by virtue of interface engineering, the interplay between ICT, electron correlation, SOC, and lattice degrees of freedom gives rise to unusual quantum states.

A series of $[mS/nL]_N$ superlattices were epitaxially grown on (001) $SrTiO_3$ substrates by pulsed laser deposition. The periodicity N is selected to keep the total thickness of each superlattice between 15 to 20 nm. Sintered Sr_2IrO_4 [41] and $LaNiO_3$ targets were ablated alternatively by a KrF excimer laser ($\lambda = 248$ nm, fluence ∼2 J·cm^{-2}) at 2 Hz and 10 Hz, respectively. A substrate temperature of 650°C and an oxygen partial pressure of 50 mTorr were maintained during deposi-
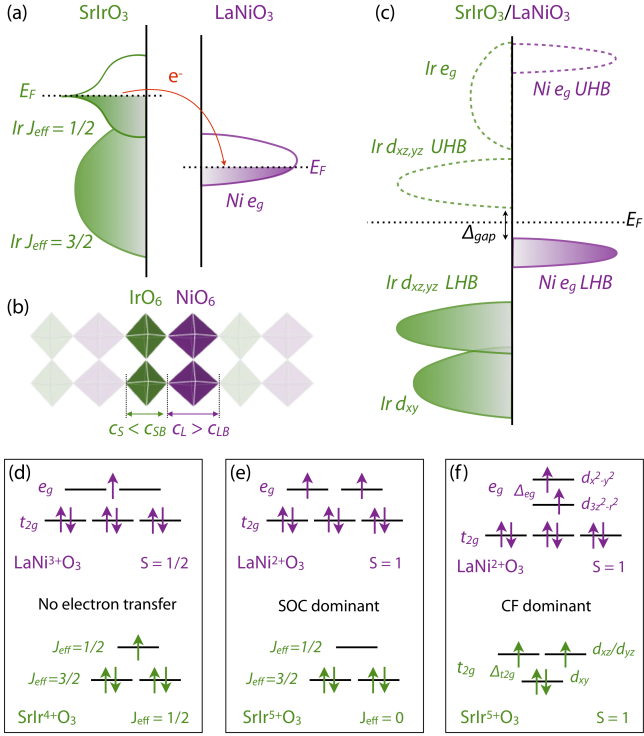
FIG. 1. (a) Density of states of bulk $SrIrO_3$ and $LaNiO_3$. (b) Schematic structure of the representative 1S/1L superlattice. Note, the compression of IrO_6 and elongation of NiO_6 octahedra is described by comparing their out-of-plane height to the bulk as $c_S < c_{SB}$, $c_L > c_{LB}$. (c) Density of states at $SrIrO_3$/$LaNiO_3$ interface. (d)-(f) Schematic energy diagrams and orbital splitting configurations of Ni and Ir in (c) bulk, (d) $SrIrO_3$/$LaNiO_3$ interface with SOC dominant, (e) $SrIrO_3$/$LaNiO_3$ interface with crystal field (CF) dominant.

FIG. 2. Resonant XAS near (a) Ni L_2 edge at 20 K and (b) Ir L_3 edge at 5 K, respectively. The blue and red curves are adapted from literatures as representative spectra of Ni^{2+} [43], Ni^{3+} [44], Ir^{4+} [41], and Ir^{5+} [45]. (c)-(d) Average oxidation state of each cation in the superlattices classified into two series: 1S/nL (n = 1, 3, 10); mS/3L (m = 1, 2, 4). Note, all superlattices are insulating except for 1S/10L, which is metallic and represented by closed dots (See Supplemental Material for transport data [42]). The dash lines are calculated values from modeling [46].

tion. Combined *in-situ* reflection-high-energy-electron-diffraction, X-ray diffraction and reciprocal space mapping confirm the high crystallinity of the samples, with the expected thickness and periodicity (See Supplemental Material [42] Fig. S1). Resonant X-ray absorption spectroscopy (XAS) and X-ray linear dichroism (XLD) measurements near Ni $L_{2,3}$ edges were taken in the luminescence yield detection mode at beamline 6.3.1 and 4.0.2 of the Advanced Light Source. Resonant X-ray magnetic circular dichroism (XMCD) near Ir $L_{2,3}$ edges were taken in the fluorescence yield mode at beamline 4IDD of the Advanced Photon Source. First-principles density functional theory (DFT) calculations were carried out on the 1S/1L superlattice using VASP [47] including both Hubbard U (within the rotationally invariant method of Liechtenstein *et al.* [48]) and SOC. The Perdew-Burke-Ernzerhof (PBE) exchange-correlation potential [49, 50] was used with projector augmented wave (PAW) potentials [51, 52] and the density of states calculations used the tetrahedral method with Blöchl corrections [53].

We begin our experimental characterization of the ICT using element-specific XAS measurements, Figs. 2(a)-(b).
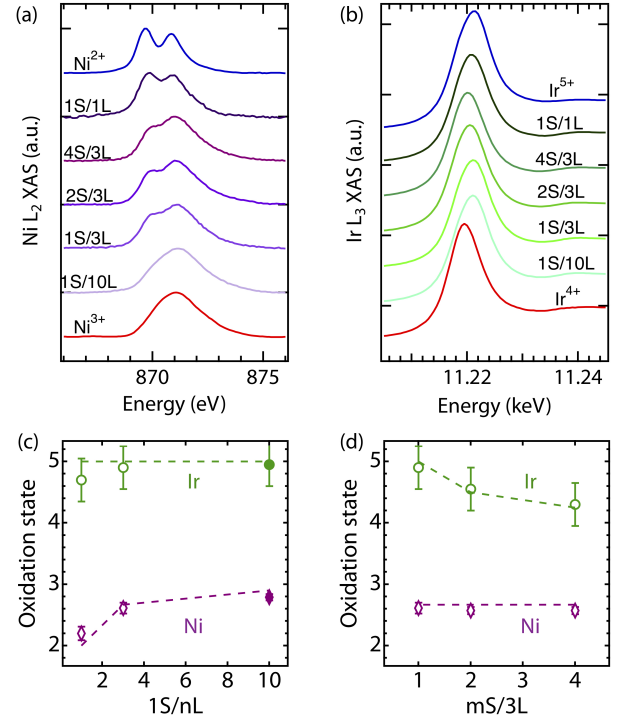
For each superlattice, the Ni L_2 edge shows a mixture of both Ni^{2+} and Ni^{3+} features and the peak position of the Ir L_3 edge shifts towards higher energy with respect to the reference peak of Ir^{4+}, indicating the Ir oxidation state increases [45]. These combined results clearly demonstrate that electrons are intrinsically transferred from Ir to Ni sites giving rise to hole(electron)-doped $SrIrO_3$($LaNiO_3$) layers, respectively. We estimate the average oxidation state of Ir by calculating the relative peak shift with respect to the positions of nominal Ir^{4+} and Ir^{5+} reference materials [45] and of Ni by spectral deconvolution of Ni L_2 XAS (Supplemental Material [42], Fig. S2). For the 1S/nL series [Fig. 2(c)], we observe the average Ir oxidation state remains almost constant at Ir^{5+}, indicating a hole-doped $SrIrO_3$ layer. The Ni oxidation state at $n = 1$ is significantly reduced from the nominal Ni^{3+} to $Ni^{2.2+}$, indicating an electron-doped $LaNiO_3$ layer; however, as n increases the oxidation state of Ni does as well, implying a lower density of electron-doped $LaNiO_3$ in the superlattices. For the mS/3L series [Fig. 2(d)], the Ir oxidation state increases from $Ir^{4.3+}$ (m
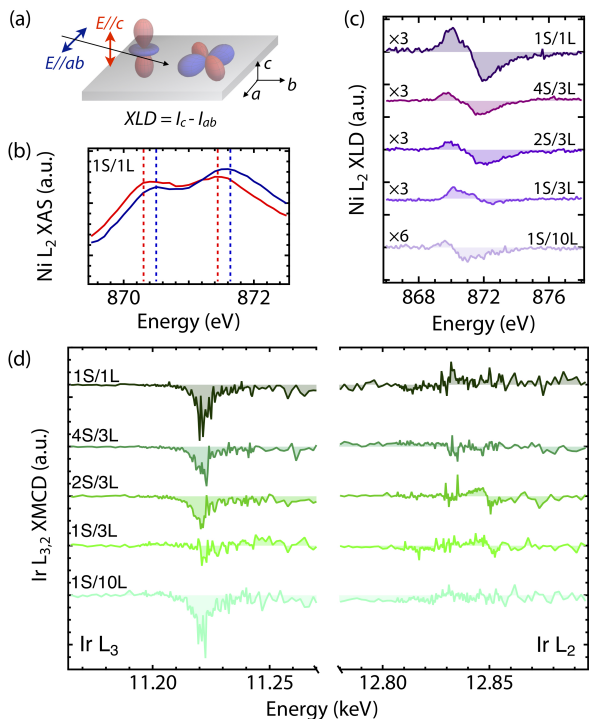
FIG. 3. (a) Schematic of XLD setup. (b) Magnified Ni L_2 XAS of the 1S/1L superlattice. The red and blue dotted lines refer to the peak positions of spectra taken with out-of-plane ($E \parallel c$) and in-plane ($E \parallel ab$) polarizations. (c) Ni L_2 XLD at 300 K. (d) Ir $L_{2,3}$ XMCD at 5 K under H = 4 T.

$= 4$) to Ir$^{4.9+}$ ($m = 1$), whereas Ni remains at approximately Ni$^{2.6+}$. This systematic variation of the oxidation state with layer thickness reflects the interfacial nature of the charge transfer between Ir and Ni. Furthermore, using a simple model assuming charge transfer across one interface [46] we find good agreement with the experimental results (see the dashed lines in Figs. 2(c)-(d)), highlighting that the charge transfer occurs only at the interface and results in an unusual electronic configuration: Ir^{4+}/Ni^{3+}→ Ir^{5+}/Ni^{2+}.

To quantify the effect of such a massive ICT on the orbital ordering and spin states, we probe the occupation of Ni e_g orbitals by XLD. As sketched in Fig. 3(a), this approach uses x-rays with different linear polarizations (i.e. in-plane $E \parallel ab$ vs. out-of-plane $E \parallel c$), which can selectively probe the valence holes on orbitals with different orientations, in our case $d_{x^2-y^2}$ vs. $d_{3z^2-r^2}$. The difference of these two spectra gives rise to the XLD signal, I_c - I_{ab}. As shown in Fig. 3(b), a representative spectrum of the 1S/1L superlattice recorded with in-plane polarization (blue curve) shifts $\sim$0.2 eV higher in energy with respect to that with out-of-plane polarization (red curve) signifying the energy of the Ni $d_{x^2-y^2}$ orbital is indeed higher than the $d_{3z^2-r^2}$ orbital with a splitting $\Delta_{e_g} \simeq 0.2$ eV [54]. Moreover, the integrated value of the 1S/1L XLD intensity is close to zero, reflecting that

TABLE I. Summary of branching ratio (BR) and sum rules analysis. M_{Ir}, M_O and M_S represent the net magnetic moment of Ir, its orbital magnetic moment, and its spin magnetic moment, respectively.

mS/nL	BR	$\langle L \cdot S \rangle$ [$\hbar^2$]	M_{Ir} [μ_B]	M_O/M_S
4/3	5.3	2.8	0.04	0.7
2/3	5.4	2.9	0.04	0.6
1/3	5.3	3.1	0.01	0.4
1/1	5.5	3.1	0.06	0.4
1/10	5.1	3.0	0.05	0.7

both orbitals are almost equally occupied [55, 56]. Note, since in this case the e_g orbitals are almost half filled, the intrinsic Jahn-Teller distortion cannot be the source of such an energy splitting. Additionally, as the degeneracy of the $d_{x^2-y^2}$ and $d_{3z^2-r^2}$ levels is known to remain unaffected in tensile-strained ultrathin LaNiO$_3$ layers [44], the effect of epitaxial strain can also be ruled out as a cause for this energy splitting. The observed splitting is, therefore, likely the result of the deformation of interfacial IrO$_6$ and NiO$_6$ octahedra caused by the ICT, leading to a significant non-cubic CF splitting. This is further supported as the XLD signal diminishes in intensity, indicating a smaller splitting, as the proportion of interfacial NiO$_6$ octahedra decreases as n increases, shown in Fig. 3(c). Since the oxidation state of interfacial Ni sites is close to Ni^{2+}, we posit the interfacial Ni has the $3d^8$ high-spin configuration ($S = 1$), favored by Hund's coupling and that the orbital ordering most likely follows the CF dominant picture with elongated NiO$_6$ octahedra, Fig. 1(f).

To investigate the presence of magnetism on iridium, we measure the XAS near the Ir $L_{2,3}$ edges using both left- and right- polarized x-rays. The spectral difference, known as the XMCD, is sensitive to the net magnetic moments of the ions. As displayed in Fig. 3(d), all samples exhibit a relatively large negative signal at the Ir L_3 edge and a markedly diminished signal at the Ir L_2 edge. Note, such a XMCD behavior is very different from the results of iridate-manganite systems, which typically show comparable intensities at the Ir $L_{2,3}$ edges with the same sign due to the predominant contribution from the orbital moments [19, 21, 57]. Branching ratio (BR) and sum rules analyses (Supplementary Material [42], Fig. S4) are applied to investigate the strength of SOC of all samples, as summarized in Table I. The presence of SOC is evident from the BR falling into the range of 5.0 - 5.5 [7, 45]. However, it is striking that the ratio of orbital moment to spin moment is rather small ($M_O/M_S \leq 0.7$; reaches the minimum at 1S/1L), largely reduced comparing to iridate-based systems in the strong SOC limit ($M_O/M_S \geq 2.0$) [57–59].

As the XMCD results clearly demonstrate the existence of a local moments on Ir, the system cannot be

in the strong SOC limit as one would expect a *non-magnetic* $J_{\text{eff}} = 0$ ground state [see Fig. 1(e)]. Furthermore, as our XLD results suggest elongated interfacial NiO_6 octahedra, we expect the adjacent IrO_6 octahedra to be compressed, removing the t_{2g} degeneracy by lowering the d_{xy} orbital. In fact, it has been recently shown that the validity of the strong SOC limit critically depends on the degree of IrO_6 octahedral distortions which can induce a non-cubic CF splitting of comparable strength [60, 61] causing strong mixing of the $J_{\text{eff}} = 1/2$ and $J_{\text{eff}} = 3/2$ states. As a result, the SOC no longer defines the energy diagram of Ir t_{2g} manifold and, instead, the CF energy scale dominates the electronic structure (see Fig. 1(f)). This scenario is consistent with all our experimental observations.

To further elucidate the microscopic details of the $SrIrO_3/LaNiO_3$ interface and the associated electronic reconstruction, we carried out first-principles calculations. As the films are coherently strained to $SrTiO_3$, we constrain the in-plane lattice constants (a and b), while allowing the c-axis to relax for a variety of tilt patterns finding that the low energy structure has the Pc (Group No. 70) symmetry. Here, the tilt pattern is akin to $a^-a^-c^-$, where tilt angle about the c-axis is different in the two materials. The results presented here include spin-orbit coupling along with $U_{\text{Ni}} = 4.6$, $U_{\text{Ir}} = 2.6$, $J_{\text{Ni}} = J_{\text{Ir}} = 0.6$, $a = b = 3.94$ Å, and a relaxed $c = 8.13$ Å. The NiO_6 octahedra, with a height of 4.22 Å, elongate along the c-axis and have a volume of 11.4 Å^3, about 9% larger than in bulk $LaNiO_3$ [62]. The IrO_6 octahedra, with a height of 3.91 Å, compresse along the c-axis and have a volume of 11.0 Å^3, similar to the bulk.

We find the Ir and Ni orbital ordering, consistent with Fig. 1(f), is intimately linked with the octahedral compression and elongation, respectively, and the associated crystal field splitting. Ni has a magnetic moment of 1.6 μ_B indicating a high-spin ($S = 1$) Ni^{2+} state and Ir a magnet moment of 0.8 μ_B indicating an orbital ordering dictated by the non-cubic crystal field splitting and not by SOC alone which would result in a non-magnetic $J_{\text{eff}} = 0$ state.

By inspecting both the band structure and the Ir and Ni d-orbital projected density of states (shown in Fig. 4), we find a semimetallic state with a very small overlap between the Ni-dominated valence band (purple) and the Ir-dominated conduction band (green). We believe this overlap can be attributed to the mistreatment of correlation effects in DFT, which often underestimates the band gap. The valence band, with Ni $d_{x^2-y^2}$ character, are the states into which the electron has been transferred. The remaining occupied Ni states (t_{2g} and $d_{3r^2-z^2}$ orbitals) are lower in energy, consistent with the crystal field splitting of an octahedron elongated along the z-axis. The unoccupied Ni e_g orbitals are well above the conduction band (supplementary Fig. S5). The conduction band is associated with the hole left from the transferred elec-
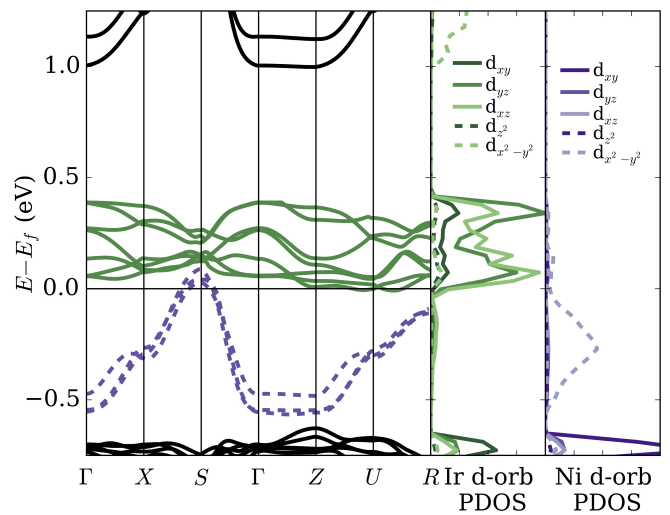

FIG. 4. Calculated band structures for 1S/1L superlattice using DFT+U with SOC included. The solid green conduction bands are dominated by Ir $d_{xz,yz}$ states where the electron was transferred from. The dashed purple valence bands are dominated by Ni $d_{x^2-y^2}$ states where the electron is transferred to. Projected density of state (PDOS) of the d-orbitals for Ir and Ni and Ir are shown on the right.

tron and is comprised of the Ir $d_{xz,yz}$ orbitals, while the remaining Ir t_{2g} orbitals are occupied and are positioned well below the valence band and the unoccupied Ir e_g orbitals above the conduction band. A checkerboard-type antiferromagnetic ordering is adopted in the Ni layers. We comment that a ferromagnetic order within the Ni layers leads to dispersive $d_{x^2-y^2}$ bands which strongly prohibits the system to become insulating (see Supplementary Material Fig. S6). Overall we find that the transferred electron localizes on Ni leading to a $S = 1$ state due to its large Hund's coupling. The NiO_6 octahedra elongate along the c-axis as a result of electron doping and in-plane constraint, compressing the IrO_6 octahedra. This stabilizes an $S = 1$ Ir state, where the large non-cubic crystal field splitting dominates the spin-orbit coupling.

In summary, we have experimentally realized a series of high quality iridate-nickelate superlattices. We observe up to a full electron transfers at $SrIrO_3/LaNiO_3$ interface from Ir to Ni site, triggering an atypical electronic and magnetic reconstruction. Unlike the vast majority of iridates where the strong SOC dominates and thus defines the ground state, in this case the interface-driven octahedral distortions induce a non-cubic crystal field splitting leading to the breakdown of the SOC picture. An unusual $S = 1$ magnetic state emerges for the Ir^{5+} ions in the superlattices. The experimental findings are well supported by the first-principles calculations, which reveal the Mott character of the band gap, determined collectively by Ir and Ni Hubbard subbands. Our findings

push past the idea of 'band bending' for ICT systems to a regime of 'band reorganization' and highlights the need for careful evaluation and possible re-interpretation of the spin-orbit driven physics in ultra-thin films and heterostructures based on $5d$ transition metal oxides.

* xiaoran.liu@rutgers.edu

[1] H. Y. Hwang, Y. Iwasa, M. Kawasaki, B. Keimer, N. Nagaosa and Y. Tokura, Nat. Mater. **11**, 103 (2012).

[2] J. Chakhalian *et al.*, Rev. Mod. Phys. **86**, 1189 (2014).

[3] P. Zubko, S. Gariglio, M. Gabay, P. Ghosez and J.-M. Triscone, Annu. Rev. Condens. Matter Phys. **2**, 141 (2011).

[4] J. Mannhart and D. G. Schlom, Science **327**, 1607 (2010).

[5] S. Stemmer and S. J. Allen, Annu. Rev. Mater. Res. **44**, 151 (2014).

[6] H. Chen and A. Millis, J. Phys.: Condens. Matter **29**, 243001 (2017).

[7] B. J. Kim *et al.*, Phys. Rev. Lett. **101**, 076402 (2008).

[8] B. J. Kim *et al.*, Science **323**, 1329 (2009).

[9] W. Witczak-Krempa *et al.*, Annu. Rev. Condens. Matter Phy. **5**, 57 (2014).

[10] Jeffrey G. Rau, Eric Kin-Ho Lee, and Hae-Young Kee, Annu. Rev. Condens. Matter Phy **7**, 195 (2015).

[11] R. Schaffer *et al.*, Rep. Prog. Phys. **79**, 094504 (2016).

[12] D. Xiao, W. Zhu, Y. Ran, N. Nagaosa and S. Okamoto, Nat. Commun. **2**, 596 (2011).

[13] J.-M. Carter, V. V. Shankar, M. A. Zeb and H.-Y. Kee, Phys. Rev. B **85**, 115105 (2012).

[14] Y. Chen, Y.-M. Lu and H.-Y. Kee, Nat. Commun. **6**, 6593 (2015).

[15] F. Wang and T. Senthil, Phys. Rev. Lett. **106**, 136402 (2011).

[16] H. Watanabe, T. Shirakawa and S. Yunoki, Phys. Rev. Lett. **110**, 027002 (2013).

[17] Z. Y. Meng, Y. B. Kim and H.-Y. Kee, Phys. Rev. Lett. **113**, 177003 (2014).

[18] X. Wan, A. M. Turner, A. Vishwanath and S. Y. Savrasov, Phys. Rev. B **83**, 205101 (2011).

[19] J. Nichols *et al.*, Nature Commun. **7**, 12721 (2016).

[20] S. Okamoto, J. Nichols, C. Sohn, S. Y. Kim, T. W. Noh and H. N. Lee, Nano Lett. **17**, 2126 (2017).

[21] D. Yi *et al.*, Phys. Rev. Lett. **119**, 077201 (2017).

[22] I. Fina *et al.*, Nature Commun. **5**, 4671 (2013).

[23] J. Matsuno, K. Ihara, S. Yamamura, H. Wadati, K. Ishii, V. V. Shankar, H.-Y. Kee, and H. Takagi, Phys. Rev. Lett. **114**, 247209 (2015).

[24] D. J. Groenendijk, N. Manca, G. Mattoni, L. Kootstra, S. Gariglio, Y. Huang, E. van Heumen, and A. D. Caviglia, Appl. Phys. Lett. **109**, 041906 (2016).

[25] D. Hirai. J. Matsuno, and H. Takagi, APL Mater. **3**, 041508 (2015).

[26] D. Yi *et al.*, PNAS. **113**, 6397-6402 (2016).

[27] J. Matsuno *et al.*, Sci. Adv. **2**, e1600304 (2016).

[28] J. H. Gruenewald *et al.*, Adv. Mater. **29**, 1603797 (2017).

[29] L. Hao *et al.*, Phys. Rev. Lett. **119**, 027204 (2017).

[30] M. L. Medarde, J. Phys.: Condens. Matter **9**, 1679 (1997).

[31] T. Mizokawa, D. I. Khomskii, and G. A. Sawatzky, Phys. Rev. B **61**, 11263 (2000).

[32] S. Johnston, *et al.*, Phys. Rev. Lett. **112**, 106404 (2014).

[33] H. Park, A.J. Millis, C.A. Marianetti, Phys. Rev. Lett. **109**, 156402 (2012).

[34] Zhicheng Zhong, and Philipp Hansmann, Phys. Rev. X **7**, 011023 (2017).

[35] T. Oka and N. Nagaosa, Phys. Rev. Lett. **95**, 266403 (2005).

[36] S. J. Moon *et al.*, Phys. Rev. Lett. **101**, 226402 (2008).

[37] H. Zhang, K. Haule, and D. Vanderbilt, Phys. Rev. Lett. **111**, 246402 (2013).

[38] K.-H. Kim, H.-S. Kim, and M.J. Han, J. Phys.: Condens. Matter **26**, 185501 (2014).

[39] M. A. Zeb and H.-Y. Kee, Phys. Rev. B **86**, 085149 (2012).

[40] Y. F. Nie *et al.*, Phys. Rev. Lett. **114**, 016401 (2015).

[41] Xiaoran Liu, Yanwei Cao, B. Pal, S. Middey, M. Kareev, Y. Choi, P. Shafer, D. Haskel, E. Arenholz, and J. Chakhalian, Phys. Rev. Mater. **1**, 075004 (2017).

[42] See Supplemental Material for additional information on structural characterizations, transport measurements and spectroscopic analysis.

[43] R. Morrow, K. Samanta, T. Saha Dasgupta, J. Xiong, J. W. Freeland, D. Haskel, and P. M. Woodward, Chem. Mater. **28**, 3666 (2016).

[44] J. Chakhalian *et al.*, Phys. Rev. Lett. **107**, 116805 (2011).

[45] M. A. Laguna-Marco, P. Kayser, J. A. Alonso, M. J. Martínez-Lope, M. van Veenendaal, Y. Choi, and D. Haskel, Phys. Rev. B **91**, 214433 (2015).

[46] The calculated average oxidation states were obtained from modeling the valence distribution within one periodicity (mS + nL) of the superlattices. In this model, the valence of Ni (Ir) in the interfacial one layer is determined to be 2+ (5+), whereas valence of the rest away from the interface is assumed to maintain the bulk values, 3+ (4+). The average oxidation state of Ni is given by $(2+3(n-1))/n$; average oxidation state of Ir is given by $(5+4(m-1))/m$.

[47] G. Kresse, J. Furthmüller, Phys. Rev. B **54**, 11169 (1996).

[48] A. Liechtenstein, V. Anisimov, J. Zaanen, Phys. Rev. B **52**, R5467 (1995).

[49] J. P. Perdew, K. Burke, M. Ernzerhof, Phys. Rev. Lett. **77**, 3865 (1996).

[50] J. P. Perdew, K. Burke, M. Ernzerhof, Phys. Rev. Lett. **78**, 1396 (1997).

[51] P. E. Blöchl, Phys. Rev. B **50**. 17953 (1994).

[52] G. Kresse, D. Joubert, Phys. Rev. B**59**, 1758 (1999).

[53] P. E. Blöchl, O. Jepsen, O. K. Andersen,Phys. Rev. B **49**, 16223 (1994).

[54] Y. Cao, X. Liu, M. Kareev, D. Choudhury, S. Middey, D. Meyers, J.-W. Kim, P. J. Ryan, J. W. Freeland, and J. Chakhalian, Nat. Commun. **7**, 10418 (2016).

[55] G. van der Laan, J. Phys. Soc. Jpn. **63**, 2393-2400 (1994).

[56] M. Wu *et al.*, Phys. Rev. B **88**, 125124 (2013).

[57] D. Yi *et al.*, Proc. Natl. Acad. Sci. U.S.A **113**, 6397 (2016).

[58] S. Fujiyama, H. Ohsumi, K. Ohashi, B. J. Kim, T. Arima, M. Takata, and H. Takagi, Phys. Rev. Lett. **112**, 016405 (2014).

[59] J.-W. Kim, Y. Choi, S. H. Chun, D. Haskel, D. Yi, R. Ramesh, J. Liu, and P. J. Ryan, Phys. Rev. Lett. **97**, 094426 (2018).

[60] X. Liu *et al.*, Phys. Rev. Lett. **109**, 157401 (2012).

[61] G. Cao, T. F. Qi, L. Li, J. Terzic, S. J. Yuan, L. E. DeLong, G. Murthy, and R. K. Kaul, Phys. Rev. Lett. **112**, 056402 (2014).

[62] F. Zuo *et al.*, Nat. Comm. **8**, 240 (2017).